

Laboratory Resolved Structure of Supercritical Perpendicular Shocks

Douglass Endrizzi¹, J. Egedal¹, M. Clark¹, K. Flanagan¹, S. Greess¹, J. Milhone¹, A. Millet-Ayala¹,
J. Olson¹, E. E. Peterson², J. Wallace¹, and C. B. Forest¹

¹Wisconsin Plasma Physics Laboratory, University of Wisconsin–Madison, 1150 University Avenue, Madison, Wisconsin 53706, USA

²Plasma Science and Fusion Center, Massachusetts Institute of Technology, NW17, 77 Massachusetts Avenue, Cambridge, Massachusetts 02139, USA

(Received 2 January 2021; revised 24 February 2021; accepted 2 March 2021; published 5 April 2021; corrected 19 April 2021)

Supermagnetosonic perpendicular flows are magnetically driven by a large radius theta-pinch experiment. Fine spatial resolution and macroscopic coverage allow the full structure of the plasma-piston coupling to be resolved in laboratory experiment for the first time. A moving ambipolar potential is observed to reflect unmagnetized ions to twice the piston speed. Magnetized electrons balance the radial potential via Hall currents and generate signature quadrupolar magnetic fields. Electron heating in the reflected ion foot is adiabatic.

DOI: 10.1103/PhysRevLett.126.145001

Collisionless shocks are ubiquitous astrophysical phenomena, appearing in diffuse plasmas wherever flows exceed sonic and Alfvénic speeds. In the heliosphere, interplanetary shocks produce gradual solar energetic particle events, and near the Earth the magnetospheric bow shock helps determine our space weather [1,2]. Such heliospheric shocks show wide variation in magnetosonic Mach number (M_{MS}) and in magnetic field orientation, which leads to a variety of dissipation mechanisms and complex kinetic physics [3]. Above a critical Mach number, ion reflection becomes a significant contributor to energy dissipation [4]. These reflected ions add a foot to the shock structure, which affects electron heating and influences the overall energy partition [5,6].

In recent years, laboratory experiments using laser generated plasma have advanced our understanding of collisionless shocks. Experiments have shown evidence for counterstreaming instabilities and even first-order Fermi acceleration [7–10]. Before high-powered lasers were available, pulsed power experiments like the theta pinch (θ pinch) made collisionless flows using magnetic pistons. Many observations first made in θ pinches were later made by spacecraft and simulations, including turbulent anomalous resistivity [11–13], specularly reflected ions [14,15], and a critical Mach number for ion reflection [16,17]. However, their short duration ($\tau_{exp} \leq \omega_{ci}^{-1}$) limited their relevance to shock formation processes rather than steady state dynamics [18]. Designed as thermonuclear experiments, θ pinches generally did not operate with plasma beta ($\beta = 2\mu_0 nT/B^2$) above one and had limited diagnostic access [19–21].

Compared to prior pinches, the Big Red Ball at the Wisconsin Plasma Physics Laboratory can make measurements of high- β super-Alfvénic flows with unprecedented detail at the microscale and simultaneous coverage of the

mesoscale structure [22]. In this Letter, we present laboratory observations of weakly magnetized laminar flows in a θ pinch with $\beta \sim 5$ and $M_{MS} \sim 3.6$. These 2D measurements reveal previously unseen features such as Hall magnetic fields, which are potentially important in reforming quasiperpendicular shocks that are recently observed to be modulated by strong Alfvénic perturbations [23]. While the normalized system size ($R \sim \rho_i$), duration ($\tau_{exp} \sim \omega_{ci}^{-1}$), and turbulence levels are all vastly smaller than in space environments, this experiment studies basic dynamics in early shock development not easily investigated *in situ* by spacecraft. We make three observations that are new or significantly advanced compared to prior experimental work: First, we confirm that the initial penetration speed of the magnetic piston is governed by the reflected ion ram pressure and that these reflected ions lead to upstream adiabatic electron heating. Next, we identify quadrupolar out-of-plane magnetic fields generated by the reflected ion cross field current. Finally, analysis of the two-fluid terms in Ohm’s law shows the current layer dynamics are governed by electron-magnetohydrodynamics (MHD). These results show how, absent anomalous resistivity, Hall physics alone couples magnetic pistons to super-Alfvénic flows and begins shock formation.

The experiment, shown in Fig. 1, consists of a large radius plasma column with a weak axial magnetic mirror field that is cylindrically compressed in a supermagnetosonic flow. An array of 18 washer guns (10 ms duration, 100 kW each [24]) produce plasma at the mirror throat, which expands into the background field ($|B_{z0}| < 0.5$ mT, mirror ratio ~ 100). Midway through the discharge, four internal toroidal coils generate a fast-rising aligned axial field that compresses the plasma (pointing in the $-\hat{z}$ direction, rise time $\tau_{1/4} \sim 70$ μ s) [25]. Measurements are

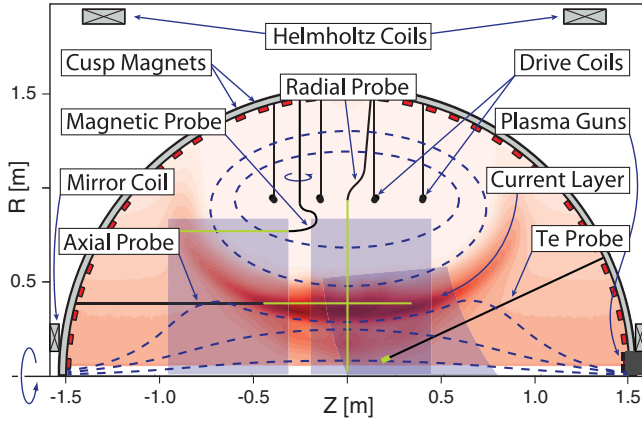


FIG. 1. Experimental cross section. Blue shaded regions show the coverage of the Langmuir probe (wedge) and magnetic probes (rectangles). The red contour map qualitatively depicts the density during θ -pinch compression, with blue dashes showing selected magnetic field lines. The four drive coils can be seen at $R = 92$, $Z = \pm 15$, ± 40 cm. Washer guns on axis supply the background plasma, which in the mirror configuration exhibits a relatively flat initial radial density profile.

made with a 5 MHz 16-tip Langmuir probe and linear arrays of 10 MHz three-axis \vec{B} coils, with resolution limited by their temporal resolution as the plasma flows past. For 100 km/s flows, they have spatial resolution of 2 and 1 cm, respectively. Both probes are jogged radially between

shots, while stationary reference probes (labeled “axial” and “radial”) align probe signals by measuring shot-to-shot variations. Subsequent experiments with toroidally spaced magnetic probes confirm good cylindrical symmetry.

The time dynamics of the implosion as reconstructed from over 200 shots are shown for a radial slice in Fig. 2. Between 10 and 16 μs , the current layer peak (dashed line) has an inward velocity of $v_l = 65$ km/s, given by its slope. The dotted line with slope $2v_l$ aligns with the leading density and temperature features. These two lines partition the experiment into four regions, which we define as the upstream, foot, current layer, and downstream, shown in the colored regions in Fig. 3. The layer and foot have M_{MS} of 3.6 and 7.2, respectively. Table I lists measurements and estimates of important scale lengths at the starred locations. While within the frame of the layer the mean free path for the upstream ions is large, within their own rest frame these ions are cold and collisional; this may damp turbulence within the layer.

The strong electric potential jump across the moving current layer reflects ions. The green line in Fig. 3 shows the steep rise in plasma potential at the layer. Ion reflection occurs as a result of the potential moving: in the layer reference frame moving at speed $-v_l$, incoming ions are reflected if their kinetic energy K_i is less than the jump in potential $\Delta\Phi_p$ across the layer. If $\Delta\Phi_p \geq 1/2m_i v_l^2 = K_i$, then in the lab frame stationary ions experience a velocity

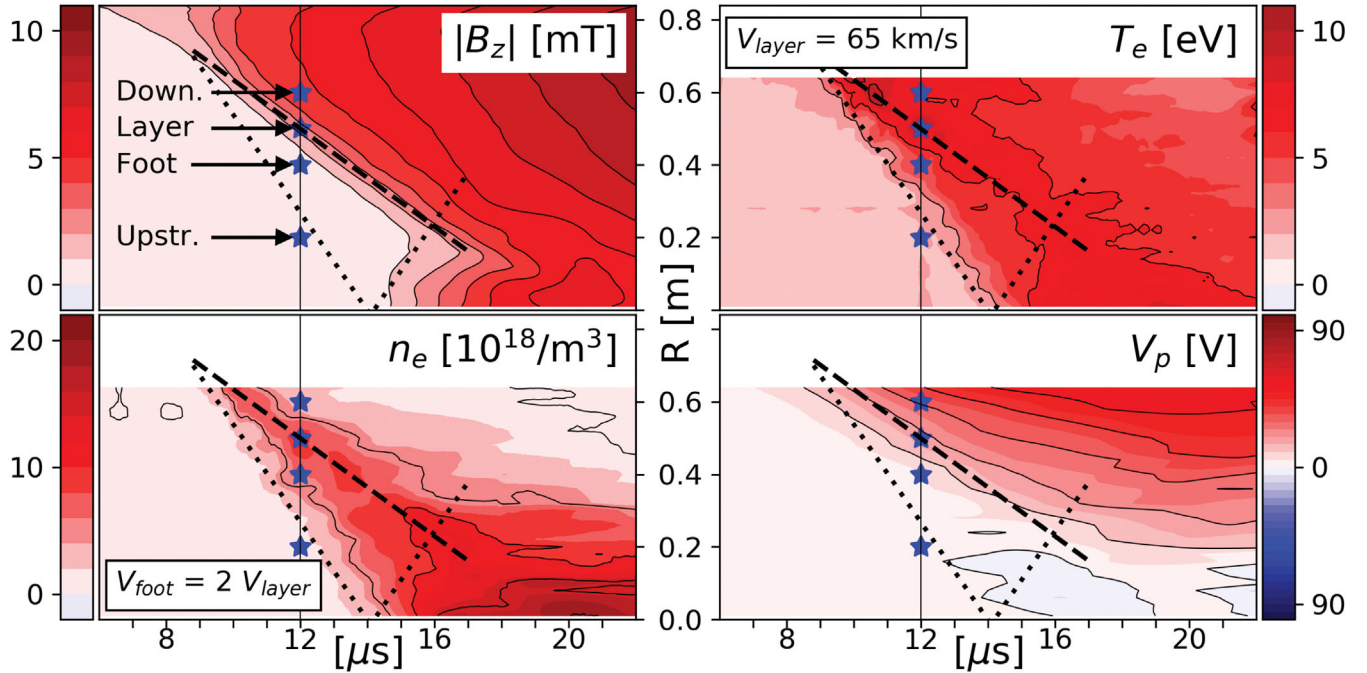


FIG. 2. Magnetic and Langmuir probe measurements of radially imploding θ pinch. This slice is taken at $z = 0.05$ m, parallel to the “radial probe” in Fig. 1. The black dashed line is a linear fit to the peak of the toroidal current layer, with the dotted lines plotted for convenience at twice the speed. Note that the dotted lines border the earliest rise in density and temperature, and that the “reflection” through the axis aligns with an increase in B_z . Values from the starred locations are listed in Table I, and data along the line at $t = 12$ μs are shown in Fig. 3. The radial electric field $E_r = -\nabla_r V_p$ is strongest along the current layer, as seen in Fig. 3. The drop in potential after 12 μs is a result of boundary conditions and electron heating in the foot, but does not affect E_r in the layer.

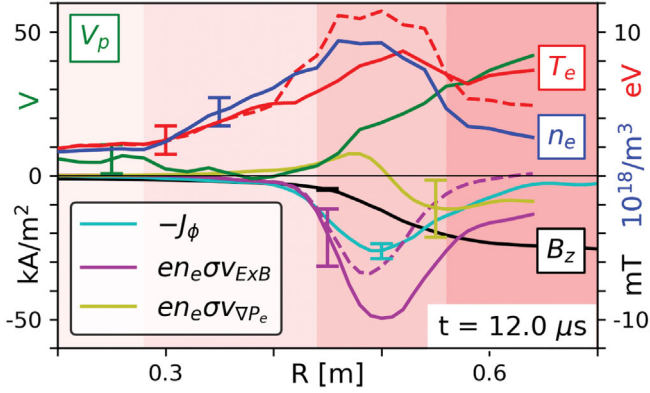


FIG. 3. R profile at $z = 0.05$ m, $t = 12 \mu\text{s}$ showing n_e , T_e , and V_p from Langmuir measurements and J_ϕ and B_z from magnetic measurements. Error bars show total error, not shot-to-shot uncertainty, which is small. The four colored areas left to right show the upstream, foot, layer, and downstream regions. The dashed red line is an adiabatic heating model, $T_e = T_{e0}(n_e/n_0)^{\gamma-1}$, for $\gamma = 2$. The factor $\sigma \equiv \omega_{ce}^2/(\nu_e^2 + \omega_{ce}^2)$ is an experimental parameter that accounts for collisional slowing [26]. The dashed magenta line estimates the sum current of the electron and ion $E \times B \hat{\phi}$ drifts, which is zero in MHD. Within error, the measured toroidal current is the sum of the $E \times B \hat{\phi}$ and electron diamagnetic drifts.

change of $-2v_l$. Figure 4(a) shows the measured linear relationship between the jump in plasma potential and the convected ion kinetic energy K_i for a variety of gases and drive voltages.

The experiment exhibits substantial ion reflection that regulates the speed of the piston. We use a 1D pressure balance model to estimate both the layer speed and the reflected ion fraction α ,

$$\frac{B_u^2}{2\mu_0} + (1 + \alpha)\rho_0 v_l^2 + P_u = \frac{B_d^2}{2\mu_0} + P_d, \quad (1)$$

TABLE I. Electron temperature, electron density, axial magnetic field, and important scale lengths at the four points in Fig. 2. Ion Larmor radii (ρ_i) and mean free paths ($\lambda_{\text{MFP}}^i = v_i/\nu_i$) are approximated using $v_i = (2T_e/m_i)^{1/2}$, $2v_l$, v_l , and v_l , respectively. The electrons are always magnetized but collisional on experimental timescales, with $\omega_{ce} > \nu_e > \tau_{\text{exp}}^{-1}$. In contrast, the reflected ions in the foot and layer are unmagnetized and collisionless, with $R_{\text{exp}} < \rho_i < \lambda_{\text{MFP}}^i$.

	Upstream	Foot	Layer	Downstream
T_e eV	2.0	5.0	8.0	6.7
n_e $10^{18}/\text{m}^3$	1.6	6.1	8.6	3.0
B_z mT	0.45	0.68	2.5	4.8
λ_{MFP}^e cm	5.1	8.4	15	30
$\rho_e = v_{\text{the}}/\omega_{ce}$ cm	1.1	1.3	0.4	0.2
λ_{MFP}^i cm	7	$> 10^3$	160	460
$\rho_i = v_i/\omega_{ci}$ cm	45	220	31	15
$d_i = c/\omega_{pi}$ cm	18	9.2	7.8	13

where subscripts u and d refer to the upstream and downstream [27,28]. The total particle inventory below the layer is constant, suggesting that within measurement error α is one. Using values from Table I (and with ρ_0 at the layer location, $r = 0.5$ m, where $n_0 = 1.0 \times 10^{18} \text{ m}^{-3}$), Eq. (1) predicts a speed of 60 ± 9 km/s, in agreement with the measured 65 ± 5 km/s. Alternatively, solving Eq. (1) for α predicts $\alpha = 0.66 \pm 0.33$. Regardless if α is 0.66 or 1.0, Eq. (1) is dominated by the ram pressure term (95% of the lhs) and the downstream magnetic pressure (75% of the rhs). The nearly constant speed is due to the initial radial density gradient conveniently balancing the increasing strength of the magnetic piston, which grows from 4.0 to 6.0 mT from 10–16 μs .

An out-of-plane quadrupolar magnetic field is observed moving ahead of the layer in Fig. 5. The unmagnetized reflected ions ($\rho_i \sim 2$ m) freely cross the weak upstream field lines while the electrons ($\rho_e \sim 1$ cm) cannot. To preserve quasineutrality, electrons from the current layer stream out to the wings of the experiment, cross field lines at some magnetic null, and then flow back to join the reflected ions. The red and blue arrows indicate the direction of these flows, which agree with the toroidal field polarity at $(r, z) = (0.6, -0.8)$ m and quadrupolar character. Further scans in the axial direction reveal parallel electric fields localized to the density and temperature gradients at the edges of the foot near $z = \pm 0.4$ m. The net

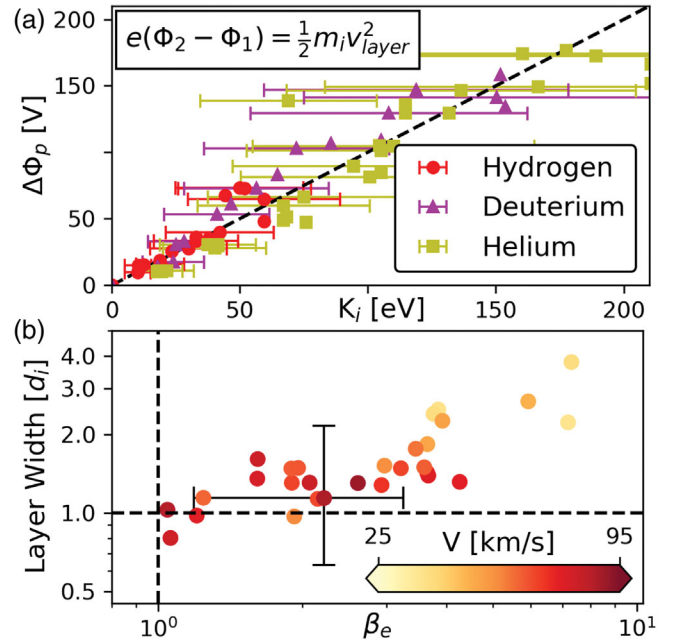


FIG. 4. (a) Plasma potential jump $\Delta\Phi_p$ vs convected ion kinetic energy $K_i = 1/2 m_i v_l^2$ showing a 1:1 relationship. $\Delta\Phi_p$ was measured a distance of $d_i/2$ on either side of the layer peak with both emissive and Langmuir probes. (b) Current layer thickness against β_e in the current layer for a variety of drive strengths in H_2 . As the magnetic piston becomes larger, the relative β_e decreases, leading to weaker ∇B drifts and a thinner current layer.

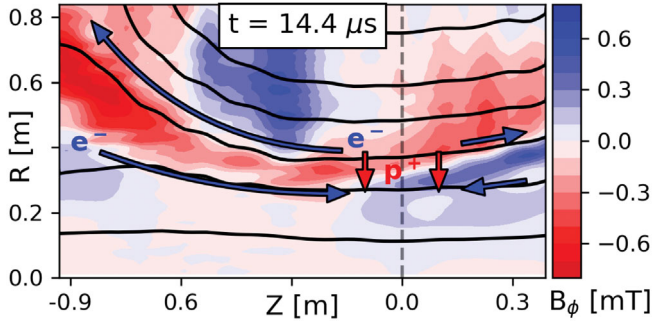


FIG. 5. Profile of toroidal magnetic field with arrows indicating direction of electron and ion flows. The red lobe at $(z, r) = (-0.8, 0.5)$ m implies current in the clockwise direction, consistent with an electron flow needed to maintain $\nabla \cdot \mathbf{J} = 0$. The peak of the toroidal current layer is near the base of the red arrows. The axial density gradient from plasma injection at the $+\hat{z}$ north pole skews the quadrupole slightly to the south.

current is a result of electrons being trapped locally by the excess reflected ion charge, not by electric fields along the entire blue path.

Electron heating in the foot is strongly correlated with the density, suggesting adiabatic heating. The dashed red line in Fig. 3 models $T_e \propto n_e^{\gamma-1}$, with $\gamma \simeq 2$ characteristic of magnetized electrons. In the layer, the adiabatic model overpredicts the electron temperature, likely because of increased thermal losses to the wall cusp. This foot region adiabatic heating is consistent with the parallel electric fields observed along the axial density gradient, which preserve quasineutrality by confining the heated electrons.

The toroidal current layer dynamics are explained by an electron-MHD model. The generalized Ohm's law neglecting electron inertia can be written

$$\mathbf{E} + \mathbf{v} \times \mathbf{B} = \eta \mathbf{J} + \frac{\mathbf{J} \times \mathbf{B}}{en_e} - \frac{\nabla \cdot \mathbf{P}_e}{en_e}. \quad (2)$$

Assuming Spitzer resistivity η_s , the resistive term is everywhere small ($E_\phi > 100\eta_s J_\phi$) and can be neglected. Examining the radial components of Eq. (2), the relative contributions of the $\mathbf{J} \times \mathbf{B}$ and $\nabla \cdot \mathbf{P}_e$ terms can be estimated from electron $E \times B$ and diamagnetic drifts, as shown in Fig. 3. The $E \times B$ drift is largest and can provide all of the necessary current, but as the ions become magnetized in the sub-Alfvénic downstream the separate $E \times B$ drifts cancel any net current. The diamagnetic drift reverses direction at the pressure peak, first opposing and then reinforcing the $E \times B$ drift. This reduces the peak current density and widens the layer. Since $v_{\nabla P_e} \propto T_{e\perp}/B^2 \propto \beta_e/n_e$, as β_e decreases the total electron drift weakens and the current layer should thin. We observe this in Fig. 4(b) and expect it is generally true in laminar high- β supercritical flows.

With these observations, the θ -pinch dynamics can be explained as follows. The applied axial magnetic field induces via Faraday's law a toroidal electric field,

beginning a radially inward $E \times B$ electron drift. The resultant charge separation produces a radial electric field that drives a second $E \times B$ electron drift in the toroidal direction. This toroidal current is not limited by the weak resistivity and grows until the applied field is canceled. On ion inertial timescales, the radial electric field accelerates ions, moving the current layer inward at a speed governed by the reflected ion ram pressure $(1 + \alpha)\rho v_i^2$. Magnetized electrons move globally to preserve quasineutrality, leading to adiabatic electron heating in the foot. These hot electrons reduce the toroidal current density, broadening the layer beyond the one d_i expected for the $T_e = 0$ case. Finally, the on-axis rise in B_z at $14 \mu\text{s}$ is from a toroidal current of reflected ions, as suggested by the dotted line in Fig. 2. The Lorentz force on the reflected ions gently deflects their radial velocity ($\rho_i \sim 2$ m). Modeling of ion trajectories confirms most are deflected in the $-\hat{\phi}$ direction producing a substantial toroidal current.

In summary, we observe the interior and large-scale structure of a laminar super-Alfvénic θ -pinch piston. The short timescale precludes ion gyration back to the layer, and so the enhanced ion reflection is not forbidden by Rankine-Hugoniot considerations [4]. Any instability growth should be strongly damped by the electron collisionality, which is large compared to the inverse layer crossing time $v_e \geq 20(d_i/v_i)^{-1}$. Furthermore, the relatively weak drifts of this experiment ($v_e \leq c_s$) are insufficient for the thin electron skin depth scale turbulent dissipation layers seen in prior pinches where $v_e \gg 10c_s$ [12,19]. Without ion gyration or turbulent dissipation, the large ion reflection $\alpha = 66\% - 100\%$ exceeds the $10\% - 25\%$ commonly observed in space [29,30]. Future measurements up to the electron plasma frequency will provide better estimates of the levels of turbulence present.

The Hall physics mechanism presented here may apply during the shock reformation process, especially when turbulence is weak or if ion reflection is high. This, and the curved experimental geometry, makes it relevant to rippled perpendicular shocks, which were first predicted in simulations [31] and recently measured by spacecraft [23,32]. As multispacecraft missions become more comprehensive, quadrupolar magnetic fields similar to this experiment may be useful for identifying nearby enhancements or focusing of reflected ions.

We acknowledge the support provided by the NSF under Grant No. DGE-1256259. In addition, this work is supported through the WIPPL User Facility under DOE fund DE-SC0018266.

- [1] H. Cane, R. McGuire, and T. Von Roseninge, Two classes of solar energetic particle events associated with impulsive and long-duration soft x-ray flares, *Astrophys. J.* **301**, 448 (1986).

- [2] D. Burgess and M. Scholer, *Collisionless Shocks in Space Plasmas: Structure and Accelerated Particles*, Cambridge Atmospheric and Space Science Series (Cambridge University Press, Cambridge, England, 2015).
- [3] C. F. Kennel, J. P. Edmiston, and T. Hada, A quarter century of collisionless shock research, in *Collisionless Shocks in the Heliosphere: A Tutorial Review*, edited by R. G. Stone and B. T. Tsurutani (American Geophysical Union (AGU), 1985), Chap. 1, pp. 1–36, <https://doi.org/10.1029/GM034p0001>.
- [4] J. Edmiston and C. Kennel, A parametric survey of the first critical mach number for a fast MHD shock, *J. Plasma Phys.* **32**, 429 (1984).
- [5] L.-J. Chen *et al.*, Electron Bulk Acceleration and Thermalization at Earth's Quasiperpendicular Bow Shock, *Phys. Rev. Lett.* **120**, 225101 (2018).
- [6] S. Schwartz, E. Henley, J. Mitchell, and V. Krasnoselskikh, Electron Temperature Gradient Scale at Collisionless Shocks, *Phys. Rev. Lett.* **107**, 215002 (2011).
- [7] L. Romagnani, S. Bulanov, and M. Borghesi, Observations of Collisionless Shocks in Laser Plasma Experiments, *Phys. Rev. Lett.* **101**, 025004 (2008).
- [8] C. Niemann *et al.*, Observation of collisionless shocks in a large current-free laboratory plasma, *Geophys. Res. Lett.* **41**, 7413 (2014).
- [9] H.-S. Park *et al.*, Collisionless shock experiments with lasers and observation of Weibel instabilities, *Phys. Plasmas* **22**, 056311 (2015).
- [10] F. Fiuzza, G. Swadling, A. Grassi *et al.*, Electron acceleration in laboratory-produced turbulent collisionless shocks, *Nat. Phys.* **16**, 916 (2020).
- [11] J. Paul, L. Holmes, and M. Parkinson, Experimental observations on the structure of collisionless shock waves in a magnetized plasma, *Nature (London)* **208**, 133 (1965).
- [12] M. Keilhacker, M. Kornherr, H. Niedermeyer, K.-H. Steuer, and R. Chodura, Experimental study of collective dissipation in shock waves for a wide range of plasma parameters (IAEA-CN-28/J-10), in *Plasma Physics and Controlled Nuclear Fusion Research Fourth Conference Proceedings 265* (International Atomic Energy Agency (IAEA), Vienna, 1971), Vol. III.
- [13] J. Scudder *et al.*, The resolved layer of a collisionless, high-beta, supercritical, quasi-perpendicular shock wave: 1. Rankine-hugoniot geometry, currents, and stationarity, *J. Geophys. Res.* **91**, 11019 (1986).
- [14] W. D. Davis, A. W. DeSilva, W. F. Dove, H. R. Griem, N. A. Krall, and P. C. Liewer, Ion heating in a high-voltage theta pinch IAEA-CN-28/J-12, in *Plasma Physics and Controlled Nuclear Fusion Research Fourth Conference Proceedings* (International Atomic Energy Agency (IAEA), Vienna, 1971), Vol. III.
- [15] G. Paschmann, N. Sckopke, S. Bame, and J. Gosling, Observations of gyrating ions in the foot of the nearly perpendicular bow shock, *Geophys. Res. Lett.* **9**, 881 (1982).
- [16] P. Phillips and A. Robson, Influence of Reflected Ions on the Magnetic Structure of a Collisionless Shock Front, *Phys. Rev. Lett.* **29**, 154 (1972).
- [17] W. Livesey, C. Russell, and C. Kennel, A comparison of specularly reflected gyrating ion orbits with observed shock foot thicknesses, *J. Geophys. Res.* **89**, 6824 (1984).
- [18] K. Papadopoulos, Microinstabilities and Anomalous Transport, in *Collisionless Shocks in the Heliosphere: A Tutorial Review*, edited by R. G. Stone and B. T. Tsurutani (American Geophysical Union (AGU), 1985), pp. 59–90, <https://doi.org/10.1029/GM034p0059>.
- [19] P. Bogen, K. J. Dietz, K. H. Dippel, E. Hintz, K. Hothker, F. Siemsen, and G. Zeyer, Shock waves and turbulent heating in low-density plasmas (IAEA-CN-28/J-11), in *Plasma Physics and Controlled Nuclear Fusion Research Fourth Conference Proceedings* (International Atomic Energy Agency (IAEA), Vienna, 1971), Vol. III.
- [20] J. W. M. Paul, C. C. Daughney, L. S. Holmes, P. T. Rumsby, A. D. Craig, E. L. Murray, D. D. R. Summers, and J. Beaulieu, Experimental study of collisionless shock waves (IAEA-CN-28/J-9), in *Plasma Physics and Controlled Nuclear Fusion Research Fourth Conference Proceedings* (International Atomic Energy Agency (IAEA), Vienna, 1971), Vol. III.
- [21] R. Merlino *et al.*, Electron and ion heating in a high-voltage toroidal theta pinch with parallel or antiparallel bias fields, *Phys. Fluids* **24**, 2358 (1981).
- [22] C. B. Forest *et al.*, The Wisconsin Plasma Astrophysics Laboratory, *J. Plasma Phys.* **81**, 345810501 (2015).
- [23] A. Johlander *et al.*, Rippled Quasiperpendicular Shock Observed by the Magnetospheric Multiscale Spacecraft, *Phys. Rev. Lett.* **117**, 165101 (2016).
- [24] G. Fiksel, A. F. Almagri, D. Craig, M. Iida, S. C. Prager, and J. S. Sarff, High current plasma electron emitter, *Plasma Sources Sci. Technol.* **5**, 78 (1996).
- [25] J. Olson *et al.*, Experimental Demonstration of the Collisionless Plasmoid Instability Below the Ion Kinetic Scale During Magnetic Reconnection, *Phys. Rev. Lett.* **116**, 255001 (2016).
- [26] F. Chen, *Introduction to Plasma Physics and Controlled Fusion*, 3rd ed. (Springer, New York, 2016).
- [27] M. Rosenbluth, Infinite conductivity theory of the pinch, U. S. Atomic Energy Commission Document, LA-1850 (1954).
- [28] D. Biskamp, Collisionless shock waves in plasmas, *Nucl. Fusion* **13**, 719 (1973).
- [29] N. Sckopke, G. Paschmann, S. J. Bame, J. T. Gosling, and C. T. Russell, Evolution of ion distributions across the nearly perpendicular bow shock: Specularly and non-specularly reflected-gyrating ions, *J. Geophys. Res.* **88**, 6121 (1983).
- [30] W. Wilkinson and S. Schwartz, Parametric dependence of the density of specularly reflected ions at quasi-perpendicular collisionless shocks, *Planet. Space Sci.* **38**, 419 (1990).
- [31] R. E. Lowe and D. Burgess, The properties and causes of rippling in quasi-perpendicular collisionless shock fronts, *Ann. Geophys.* **21**, 671 (2003).
- [32] E. L. M. Hanson, O. V. Agapitov, F. S. Mozer, V. Krasnoselskikh, S. D. Bale, L. Avanov, Y. Khotyaintsev, and B. Giles, Cross-shock potential in rippled versus planar quasi-perpendicular shocks observed by MMS, *Geophys. Res. Lett.* **46**, 2381 (2019).

Correction: The NSF grant information contained an error and has been remedied.